京都大学防災研究所年報 第43号 B-2 平成12年4月
Annuals of Disas. Prev. Res. Inst., Kyoto Univ., No. 43 B-2, 2000

Analysis of Partially Drained Behaviour of Saturated Soil Deposits Subjected to Earthquake Shaking

Hayoung KIM* and Hideo SEKIGUCHI

* Toyo Construction Co., Ltd., Japan

Synopsis

This paper describes results of dynamic response analyses of horizontal saturated soil layers subjected to vertically propagating SH waves. Formulations are made under two-dimensional conditions for wider use, and quasi-one dimensional analysis procedure is then worked out by using layer elements in order to describe seismic simple shear in a simple yet theoretically consistent manner. The analysis procedure incorporates modelling of cyclic plasticity of soils for reproducing contractant soil behaviour under cyclic shearing. The way in which contractancy contributes to seismic settlement of a saturated sand layer subject to earthquake shaking is explored, with proper consideration of the effects of partial drainage.

Keywords: cyclic plasticity; liquefaction; partial drainage; seismic settlement; simple shear

1. Introduction

Extensive damage occurred to the composite breakwaters in the port of Kobe due to the 1995 Hyogoken-Nambu earthquake (Port Bureau Ministry of Transport et al., 1997; Sekiguchi et al., 1996). The maximum settlement observed was 2.6m at breakwater No. 7 in Kobe Port. This fact emphasizes the need to consider earthquake–induced deformation of such marine gravity structures in the revision of current design practices.

Many studies have been performed along this line using numerical analysis and physical modelling. Jafarzadeh and Yanagisawa (1995) performed unidirectional shaking table tests on level ground models in a $1g$ gravitational field. Their test results indicate that permeability of saturated sands should be an important factor in seismic settlement predictions. Higuchi et al. (1995) performed a series of centrifuge shaking table tests on level ground models of loose, saturated Toyoura sand (Dr=45%). A saturated sand deposit,

in the case where viscous scaling was introduced, underwent liquefaction at all depths. However, an identical saturated sand deposit without viscous scaling (the pore fluid was water) liquefied at shallow soil depths only. The ground surface settlements in the experiments using water as the pore fluid were lager than those in the experiments conducted with viscous scaling introduced. These test results emphasize the importance of determining permeability to precisely predict the magnitude and rate of soil settlement induced by earthquake shaking. A particular program in the VELACS Project (Arulannandan, K. and Scott, R. F., 1993) dealt with level ground responses under vertically propagating SH waves, and centrifuge shaking table tests were performed and compared to "before–event" numerical predictions. However, the prediction of seismic settlement proved to be difficult to predict consistently with other dynamic soil responses.

The present study was motivated by seismic settlement studies including those mentioned above. The organization of this paper is as follows. In Section 2, a plane-strain seismic analysis program for two-phase medium is developed. Layer element modelling with zero lateral strain condition satisfied, will then be made. Section 3 reviews an elasto-plastic constitutive model by Pastor et al.(1990) and introduces a plane–strain version of it. Section 4 describes results of a series of finite element analyses performed. Conclusions obtained in the present paper are summarized in section 5.

2. Numerical formulation for two-phase medium

This section describes a set of governing equations and the corresponding finite-element discretization procedure. Compressive stresses and compressive strains are taken as positive.

2.1 Governing equations

We subsequently describe a set of equations that govern the behaviour of two–phase media(Zienkiewicz, O.C. et al., 1980; Simon, B. R. et al., 1984).

Equations of motion

Let σ_{ij} be total stress and let σ'_{ij} be effective stress. It then follows that

$$\sigma_{ij} = \sigma'_{ij} + p\delta_{ij} \tag{1}$$

where p is pore fluid pressure and δ_{ij} is Kronecker's delta.

The equations of motion can be expressed as

$$\rho\ddot{u}_i + \rho_f\ddot{w}_i = -\sigma_{ji,j} + \rho b_i \tag{2}$$

where b_i is the body force and $\rho = (1-n)\rho_s + n\rho_f$. Here ρ_s is the density of the solid particle, ρ_f is the density of the pore fluid, $\ddot{w}_i$ is the averaged relative acceleration of pore fluid to the solid skeleton and is equal to $n(\ddot{v}_i - \ddot{u}_i)$. Note here that n is the porosity, $\ddot{v}_i$ is the acceleration of the pore fluid and $\ddot{u}_i$ is the acceleration of the solid.

Substituting Eq. (1) into Eq. (2) for σ_{ij} yields

$$\rho\ddot{u}_i + \rho_f\ddot{w}_i = -\sigma'_{ji,j} - p_{,i} + \rho b_i \tag{3}$$

If the relative acceleration of the pore fluid $\ddot{w}_i$ is negligible compared with $\ddot{u}_i$, then Eq. (3) can be simplified to

$$\rho\ddot{u}_i = -\sigma'_{ji,j} - p_{,i} + \rho b_i \tag{4}$$

Continuity equation

The storage equation relevant to soil with a compressible pore fluid may be expressed as

$$\dot{w}_{i,i} = -\dot{u}_{i,i} - \frac{n}{K_f}\dot{p} \tag{5}$$

where K_f is the bulk modulus of the pore fluid.

Generalized Darcy equation for pore fluid flow can be expressed as

$$\rho_f\ddot{v}_i = -p_{,i} - \frac{\rho_f g}{k}\dot{w}_i + \rho_f b_i \tag{6}$$

where g and k are the acceleration of gravity and the coefficient of permeability respectively.

Use of the relation: $\ddot{v}_i = \ddot{w}_i/n + \ddot{u}_i$ in Eq. (6) yields

$$\rho_f\ddot{u}_i + \frac{\rho_f}{n}\ddot{w}_i = -p_{,i} - \frac{\rho_f g}{k}\dot{w}_i + \rho_f b_i \tag{7}$$

If $\ddot{w}_i$ is neglected, Eq. (7) becomes

$$\rho_f\ddot{u}_i = -p_{,i} - \frac{\rho_f g}{k}\dot{w}_i + \rho_f b_i \tag{8}$$

Taking divergence on both sides of Eq. (8) yields

$$\rho_f \ddot{u}_{i,i} = -p_{,ii} - \frac{\rho_f g}{k}\dot{w}_{i,i} \tag{9}$$

By substituting Eq. (5) into Eq.(9) for $\dot{w}_{i,i}$, it follows that

$$\rho_f \ddot{u}_{i,i} = -p_{,ii} + \frac{\rho_f g}{k}(\dot{u}_{i,i} + \frac{n}{K_f}\dot{p}) \tag{10}$$

2.2 Finite-element discretization

Strain rates $\dot{\varepsilon}_{ij}$ are defined in terms of displacement velocities of soil as follows.

$$\dot{\varepsilon}_{ij} = -\frac{1}{2}(\dot{u}_{i,j} + \dot{u}_{j,i}) \tag{11}$$

Let $\{\Delta u\}$ be the displacement increments at a generic point in a given finite element. Let $\{\Delta u_N\}$ be the displacement increments at nodes of that element. It then follows that

$$\{\Delta u\} = [N]\{\Delta u_N\} \tag{12}$$

where $[N]$ is shape functions.

Based on Eq. (12), the strain increments $\{\Delta\varepsilon\}$ and the volumetric strain increment $\Delta\varepsilon_v$ at a generic point in a finite element may be given by

$$\{\Delta\varepsilon\} = [B]\{\Delta u_N\} \tag{13}$$

$$\Delta\varepsilon_V = \{B_V\}^T\{\Delta u_N\} \tag{14}$$

where $[B]$ and $\{B_V\}$ respectively are the strain–displacement matrix and the volumetric strain–displacement vector. A superscript T denotes transpose of a vector or a matrix.

Elastoplastic constitutive relations of the soil skeleton may be expressed as

$$\dot{\sigma}'_{ij} = D_{ijkl}\dot{\varepsilon}_{kl} \tag{15}$$

where D_{ijkl} represents the coefficients of tangent stiffness matrix that generally depend on the current effective stress state as well as the plastic strain and stress histories.

Using the principle of virtual work, Eq. (3) may be expressed in incremental form:

$$[M_{UU}]\{\Delta\ddot{u}_N\} + [K_{UU}]\{\Delta u_N\} + [K_{UP}]\Delta p = \{\Delta Q\} \tag{16}$$

in which

$$[M_{UU}] = \int_V [N]^T \rho [N] dV \tag{17}$$

$$[K_{UU}] = \int_V [B]^T [D][B] dV \tag{18}$$

$$[K_{UP}] = \int_V [B]_V dV \tag{19}$$

$$\{\Delta Q\} = \int_A [N]^T \{\Delta T\} dA + \int_V [N]^T \rho \{\Delta b\} dV \tag{20}$$

where ΔT is the surface traction increment, Δb is the body force increment.

The process of deriving Eq. (16) is described in Appendix A1 of this paper.

Eq. (10) may be discretized using finite difference scheme(Akai and Tamura,1976) as follows.

$$[M_{PU}]\{\Delta\ddot{u}_N\} + [C_{PU}]\{\Delta\dot{u}_N\} + [C_{PP}]\Delta\dot{p} + \sum(\alpha_i \Delta p_i) + [K_{PP}]\Delta p = 0 \tag{21}$$

in which

$$[M_{PU}] = \frac{k}{g}(\int_V [B_V] dV) \tag{22}$$

$$[C_{PU}] = -(\int_V [B_V] dV) \tag{23}$$

$$[C_{PP}] = -(\int_V \frac{n}{K_f} dV) \tag{24}$$

$$[K_{PP}] = -\sum \alpha_i \tag{25}$$

where

$$\alpha_i = \frac{k}{\rho_f g}(\frac{S_i}{L_i}). \tag{26}$$

For the definition of S_i and L_i, reference can be made to Fig. A1 in the appendix.

The process of deriving Eq. (21) is described also in Appendix A2.

If the bulk modulus of the pore fluid $K_f \to \infty$, Eq. (21) can be rewritten as follows.

$$[M_{PU}]\{\Delta\ddot{u}_N\} + [C_{PU}]\{\Delta\dot{u}_N\} + \sum(\alpha_i \Delta p_i) + [K_{PP}]\Delta p = 0 \tag{27}$$

In order to solve Eqs. (16) and (27), it was found convenient to apply Newmark's β method to displacement increments and to excess pore pressure increments. Namely,

$$\begin{Bmatrix} \Delta\dot{u} \\ \Delta\dot{p} \end{Bmatrix} = \frac{\gamma}{\beta\Delta t}\begin{Bmatrix} \Delta u \\ \Delta p \end{Bmatrix} - \frac{\gamma}{\beta}\begin{Bmatrix} \dot{u}_t \\ \dot{p}_t \end{Bmatrix} + (1-\frac{\gamma}{2\beta})\Delta t\begin{Bmatrix} \ddot{u}_t \\ \ddot{p}_t \end{Bmatrix} \quad (28)$$

$$\begin{Bmatrix} \Delta\ddot{u} \\ \Delta\ddot{p} \end{Bmatrix} = \frac{1}{\beta\Delta t^2}\begin{Bmatrix} \Delta u \\ \Delta p \end{Bmatrix} - \frac{1}{\beta\Delta t}\begin{Bmatrix} \dot{u}_t \\ \dot{p}_t \end{Bmatrix} - \frac{1}{2\beta}\begin{Bmatrix} \ddot{u}_t \\ \ddot{p}_t \end{Bmatrix} \quad (29)$$

where γ and β are Newmark's parameters.

Substituting Eqs. (28) and (29) into Eqs. (16) and (27) yields the following:

$$\left[\frac{1}{\beta\Delta t^2}[M_{UU}]+[K_{UU}]\right]\{\Delta u_N\}+[K_{UP}]\Delta p = \{\Delta Q\}+\frac{1}{\beta\Delta t}[M_{UU}]\{\dot{u}_t\} + \frac{1}{2\beta}[M_{UU}]\{\ddot{u}_t\} \quad (30)$$

and

$$\left[\frac{1}{\beta\Delta t^2}[M_{PU}]+\frac{\gamma}{\beta\Delta t}[C_{PU}]\right]\{\Delta u_N\} +[K_{PP}]\Delta p+\sum(\alpha_i\Delta p_i) = \left(\frac{1}{2\beta}[M_{PU}]+(\frac{\gamma}{2\beta}-1)\Delta t[C_{PU}]\right)\{\ddot{u}_t\} + \left(\frac{1}{\beta\Delta t}[M_{PU}+\frac{\gamma}{\beta}[C_{PU}]\right)\{\dot{u}_t\} \quad (31)$$

Equations (30) and (31) that hold for each of the finite elements, may be assembled to give the governing equations for an entire system. Namely,

$$\left[\frac{1}{\beta\Delta t^2}[M]+\frac{\gamma}{\beta\Delta t}[C]+[K^*]\right]\begin{Bmatrix} \Delta u \\ \Delta p \end{Bmatrix} = \begin{Bmatrix} \Delta Q \\ 0 \end{Bmatrix} + \left[\frac{1}{\beta\Delta t}[M]+\frac{\gamma}{\beta}[C]\right]\begin{Bmatrix} \dot{u}_t \\ \dot{p}_t \end{Bmatrix} + \left[\frac{1}{2\beta}[M]+(\frac{\gamma}{2\beta}-1)\Delta t[C]\right]\begin{Bmatrix} \ddot{u}_t \\ \ddot{p}_t \end{Bmatrix} \quad (32)$$

where

$$[M] = \begin{bmatrix} [M_{UU}] & 0 \\ [M_{PU}] & 0 \end{bmatrix}$$

$$[C] = \begin{bmatrix} 0 & 0 \\ [C_{PU}] & 0 \end{bmatrix}$$

$$[K^*] = \begin{bmatrix} [K_{UU}] & [K_{UP}] \\ 0 & [K^*_{PP}] \end{bmatrix} \quad (33)$$

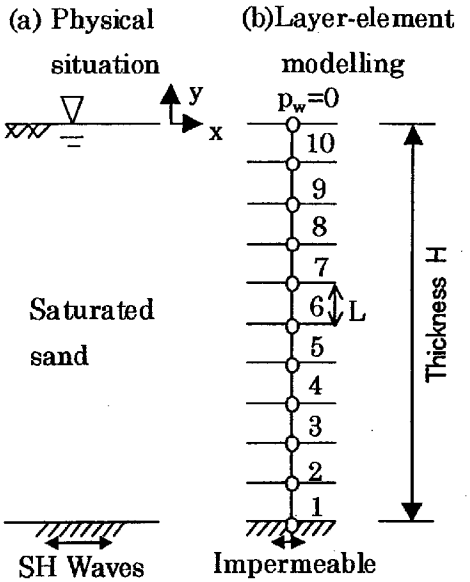

Fig. 1 Layer element modelling

Note in Eq. (33) that $[K^*_{PP}]$ represents the permeability matrix.

2.3 Quasi-one dimensional modelling

Consider that a layer of saturated sand of infinite lateral extent is subjected to vertically propagating SH waves, under partially drained conditions(Fig. 1). Under these assumptions, the seismic behaviour of the level ground turns out to be cyclic simple shear($\Delta\varepsilon_{xx}=0$), under partially drained condition.

The governing equations described earlier should be applicable to solving this type of problem as well. However, with conventional quadrilateral finite elements, it was found difficult to satisfy simple shear conditions. Thus we have introduced layer element modelling in such a way that zero lateral strain conditions are always satisfied under shearing. In essence, the strain increments may be related to the displacement increments as follows.

$$\begin{Bmatrix} \Delta\varepsilon_{xx} \\ \Delta\varepsilon_{yy} \\ \Delta\gamma_{xy} \end{Bmatrix} = [B]\begin{Bmatrix} \Delta u_i \\ \Delta v_i \\ \Delta u_j \\ \Delta v_j \end{Bmatrix} \quad (34)$$

where

$$[B] = \frac{1}{L}\begin{bmatrix} 0 & 0 & 0 & 0 \\ 0 & -1 & 0 & 1 \\ -1 & 0 & 1 & 0 \end{bmatrix} \quad (35)$$

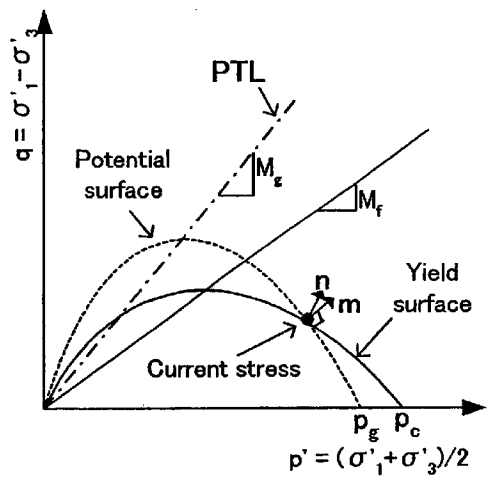

Fig. 2 Yield and potential surfaces

where L is height of layer element (Fig. 1). Note that the first row of the $[B]$ matrix permits $\Delta\varepsilon_{xx}$ to be always zero.

3. Constitutive equations

An elastoplastic constitutive model proposed by Pastor et al.(1990) was incorporated into the analysis procedure described in the preceding sections. More specifically, a plane-strain version of the Pastor et al. model was used herein. The theoretical features of the model will be outlined below, together with illustrating simulations of soil-element behaviour.

3.1 Elastoplastic constitutive modelling

The ratio between the plastic volumetic increment $d\varepsilon_v^p$ and the plastic deviatoric increment $d\varepsilon_s^p$ may conveniently be related to the effective stress ratio η as follows.

$$\frac{d\varepsilon_v^p}{d\varepsilon_s^p} = (1+\alpha)(M_g - \eta) \tag{36}$$

where $\eta = q/p'$, α is a material constant, M_g is a material constant representing the slope of the phase transformation line(PTL), $p' = (\sigma_1' + \sigma_3')/2$ and $q = \sigma_1 - \sigma_3$.

The direction of the plastic strain increment may be expressed in terms of a unit normal, $\boldsymbol{m}_L$, that is defined by

$$\boldsymbol{m}_L = \frac{1}{\sqrt{(d\varepsilon_v^p)^2 + (d\varepsilon_s^p)^2}} \begin{pmatrix} d\varepsilon_v^p \\ d\varepsilon_s^p \end{pmatrix}$$

$$= \frac{1}{\sqrt{1+d_g^2}} \begin{pmatrix} d_g \\ 1 \end{pmatrix} \tag{37}$$

where $d_g \equiv d\varepsilon_v^p/\varepsilon_s^p$.

Also, one can introduce a unit normal $\boldsymbol{n}$ to the yield surface($f = 0$) such that

$$\boldsymbol{n} = \frac{1}{\sqrt{1+d_f^2}} \begin{pmatrix} d_f \\ 1 \end{pmatrix} \tag{38}$$

where

$$d_f \equiv (1+\alpha)(M_f - \eta) \tag{39}$$

Here M_f is a material parameter.

The yield and plastic potential surfaces obtainable from the $\boldsymbol{n}$ and $\boldsymbol{m}$ vectors are of the following form:

$$f = q - M_f p' \left(1 + \frac{1}{\alpha}\right) \left\{1 - \left(\frac{p'}{p_c}\right)^{\alpha}\right\} = 0 \tag{40}$$

$$g = q - M_g p' \left(1 + \frac{1}{\alpha}\right) \left\{1 - \left(\frac{p'}{p_g}\right)^{\alpha}\right\} = 0 \tag{41}$$

These two surfaces passing through the current stress point are illustrated in Fig. 2. The parameters marked p_c and p_g represent the points where the yield and potential surfaces meet the p' co-ordinate axis.

The criteria of loading and unloading read

$$\boldsymbol{n} \cdot d\boldsymbol{\sigma}' > 0 \quad (\textit{loading})$$
$$\boldsymbol{n} \cdot d\boldsymbol{\sigma}' = 0 \quad (\textit{neutral loading})$$
$$\boldsymbol{n} \cdot d\boldsymbol{\sigma}' < 0 \quad (\textit{unloading})$$

Plastic modulus H_L for loading takes the following form:

$$H_L = H_0 \cdot p' \cdot \left(1 - \frac{\eta}{\eta_f}\right)^4 \cdot \left\{1 - \frac{\eta}{M_g} + \beta_0\beta_1 \exp(-\beta_0\xi)\right\} \cdot \left(\frac{\zeta_{max}}{\zeta}\right)^{\gamma_D} \tag{42}$$

where $H_o, \eta_f, \beta_0, \beta_1$ and γ_D are material constants. Parameter $\xi (= \int |d\varepsilon_s^p|)$ is the accumulated deviatoric plastic strain. Symbol ζ denotes a mobilized stress function and is defined by

$$\zeta = p'\{1 - \left(\frac{1+\alpha}{\alpha}\right)\frac{\eta}{M}\}^{-1/\alpha} \tag{43}$$

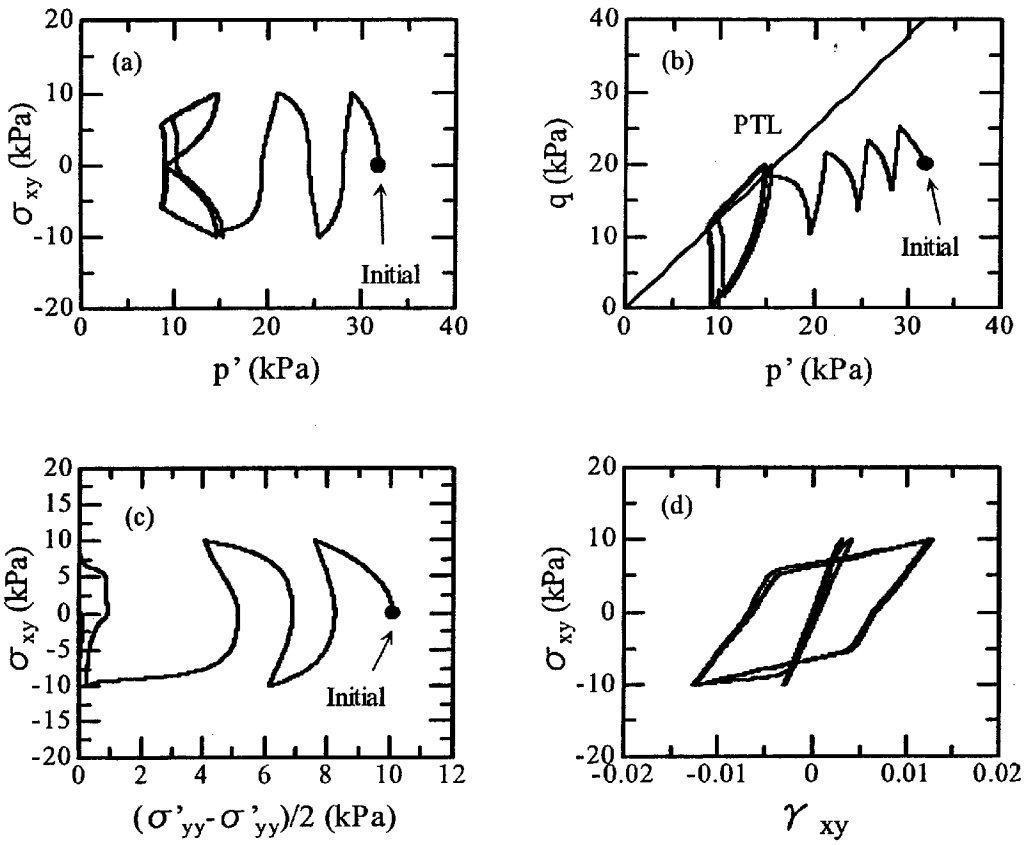

Fig. 3 Predicted performance for undrained cyclic simple shear

An important feature of actual sand behaviour is the occurrence of contractive volume changes under unloading. Also, unloading from a high stress ratio results in large plastic straining. Plastic modulus H_U for unloading is thus introduced and is described in terms of the stress ratio η_u at the starting point of unloading. That is to say,

$$H_U = \begin{cases} H_{U0}\left(\dfrac{M_g}{\eta_u}\right)^{\gamma_U} & for \left|\dfrac{M_g}{\eta_u}\right| > 1 \\ H_{U0} & for \left|\dfrac{M_g}{\eta_u}\right| \leq 1 \end{cases} \tag{44}$$

where

$$\eta_u = \left(\frac{q}{p'}\right)_u \tag{45}$$

The direction of plastic straining during unloading, $\boldsymbol{m}_U$, has been selected in such a way as to permit contractive soil behaviour to occur under unloading. Namely,

$$\boldsymbol{m}_U = \frac{1}{\sqrt{1+d_g^2}}\begin{pmatrix} -|d_g| \\ 1 \end{pmatrix} \tag{46}$$

The constitutive relations can finally be expressed in the following form:

$$\dot{\sigma}_{ij} = (L\delta_{ij}\dot{\varepsilon}_{kk} + 2G\dot{\varepsilon}_{ij} - [(L+G)d_g\delta_{ij} + \frac{2\sigma_{ij} - \delta_{ij}\sigma'_{kk}}{q}2G] \tag{47}$$

$$\cdot\frac{[(L+G)d_f\delta_{kl} + \frac{2\sigma_{kl} - \delta_{kl}\sigma'_{kk}}{q}2G]}{H||\boldsymbol{n}|| \cdot ||\boldsymbol{m}|| + (L+G)d_f d_g + 4G})\,\dot{\varepsilon}_{kl} \tag{48}$$

3.2 Illustrating element simulations

Simulations for undrained and drained cyclic simple shear of imaginary samples of saturated sand were performed. The constitutive parameters used are listed in Table 1. The values of the initial effective mean stress $(\sigma'_1 + \sigma'_3)/2$ and initial deviator stress $(\sigma'_1 - \sigma'_3)$ were arbitrarily chosen at 31.92 kPa and 20.17 kPa.

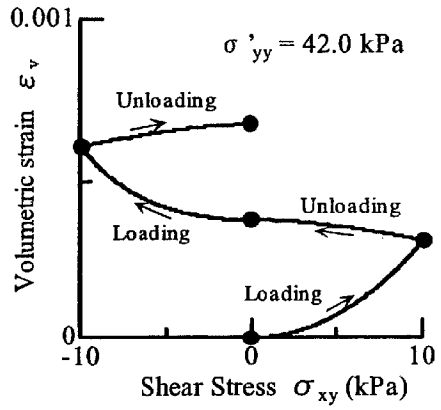

Fig. 4 Developments of volumetric strain in drained cyclic simple shear

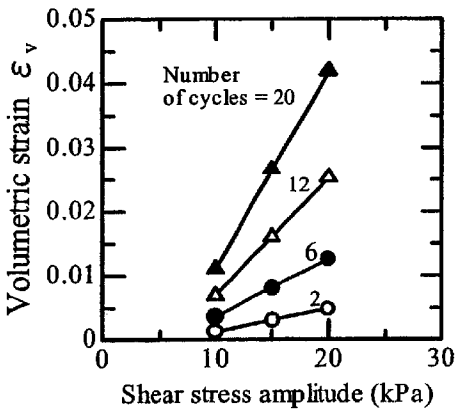

Fig. 5 Relationship between volumetric strain and shear stress amplitude in drained cyclic simple shear

Undrained cyclic simple shear

A specimen of saturated sand was subjected to undrained cyclic simple shear as shown in Fig. 3. It is seen that the mean effective stress p' decreased significantly with increasing number of shearing cycles.

Drained cyclic simple shear

An identical specimen of saturated sand was subjected to drained cyclic simple shear. The predicted volumetric strain versus shear stress curve is shown in Fig. 4 for the first one complete cycle. Volumetric strain developed throughout the process of shearing, causing the soil to gradually contract even during unloading. Note that this predicted pattern can capture the essential aspects of actual sand behaviour(Tatsuoka and Ishihara, 1974).

Table 1 Constitutive parameters

M_g	M_f	α	β_0	β_1	H_0	H_{u0} (kPa)	γ_d	γ_u
1.26	0.6	0.45	4.0	0.2	1250	8000	2	4

Table 2 Material parameters

γ' (kN/m^3)	γ_w (kN/m^3)	e_0	K_0
9.34	9.8	0.736	0.52

Table 3 Analyses performed

Case No.	Permeability $k(m/s)$
1	0 (Undrained)
2	6.6×10^{-7}
3	6.6×10^{-5}
4	3.3×10^{-4}
5	3.3×10^{-3}
6	8.8×10^{-2}
7	1.0×10^{-2}
8	3.3×10^{-1}
9	16.5

The predicted relationships between volumetric strain and shear stress amplitude are shown in Fig. 5 for four different numbers of loading cycles. Note that for a given shear stress amplitude, volumetric strain ε_v increased linearly with increasing number of cycles.

4. Predicted behaviour of level ground under earthquake shaking

This section describes results from quasi–one dimensional finite element analyses of elastoplastic soil responses under earthquake shaking.

4.1 Problem definition

Suppose that a horizontal saturated sand layer of a thickness H=10m with a uniform density (Dr= 40%) is subject to SH waves (see Fig. 1).

The hydraulic boundary conditions imposed are such that the soil layer rests on the impermeable base and the pore fluid drains freely from the ground surface.

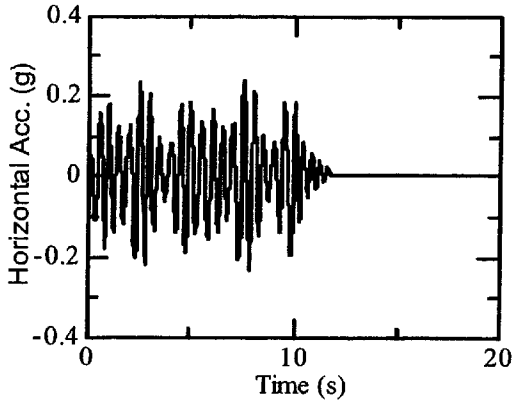

Fig. 6 Input accelerogram

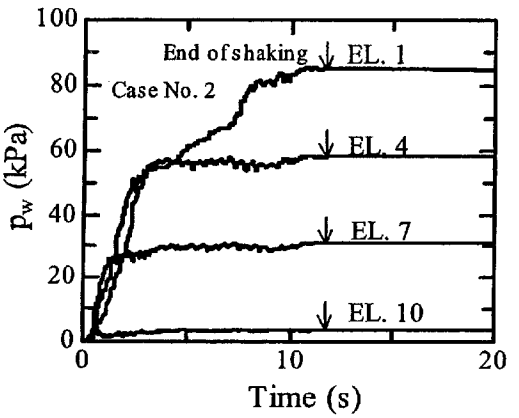

Fig. 7 Time histories of excess pore pressures in case 2

The constitutive parameters and material parameters used in the present case studies are shown in Tables 1 and 2. We selected these parameters in view of the material properties of Nevada sand that was used in the VELACS Project. In order to investigate the effects of partial drainage, the permeability was varied over a wide range (Table 3).

The time history of input horizontal acceleration is shown in Fig. 6. The main motion was 20 loading cycles at a dominant frequency of 2Hz, with a peak acceleration of $0.23g$. Time increments Δt in analyses were selected as follows: 0.002s during main motion and 10s during consolidation after the cessation of earthquake shaking.

4.2 Predicted results

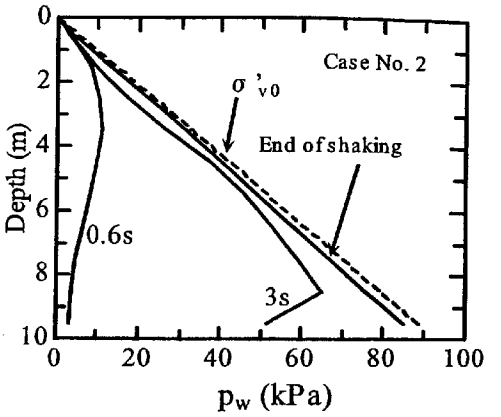

Fig. 8 Variations of excess pore pressures with depth in case 2

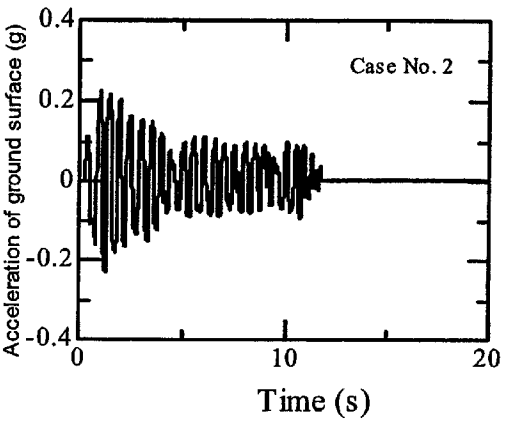

Fig. 9 Time history of surface acceleration

(1) Soil responses during main shaking

The time histories of predicted excess pore pressures in Case 2 are shown in Fig. 7. The excess pore pressures increased markedly with increasing loading cycle. The variations of excess pore pressures with depth in Case 2 are shown in Fig. 8 at various times. The excess pore pressures at shallow soil depths became very close to the initial vertical effective stress versus depth line at the end of shaking.

The acceleration amplitude at the ground surface showed a peak in the early stage of the main motion and thereafter decreased gradually with time.

The variations of excess pore pressures in Case 8 ($k = 3.3\times10^{-1}m/s$) with depth are shown in Fig. 10. The excess pore pressures were very small in magnitude because of the large permeability adop-

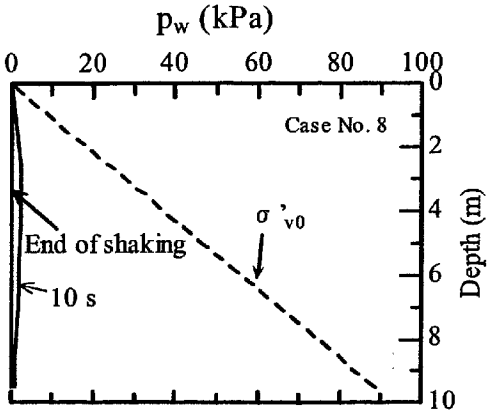

Fig. 10 Variations of excess pore pressures in case 8

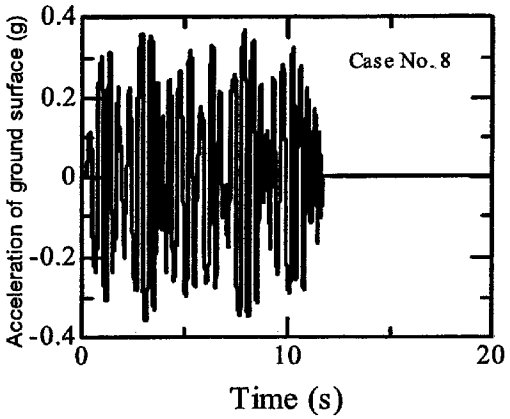

Fig. 11 Time history of surface acceleration in case 8

ted. The ground surface acceleration response in Case 8 is shown in Fig. 11. The ground surface accelerations were amplified to give a peak acceleration of 1.5 times as large as that of the input acceleration.

Surface settlement–time histories in four representative cases are depicted in Fig. 12. In the case with permeability $k = 3.3 \times 10^{-1} m/s$, the settlement developed only during the main shaking, with no consolidation settlement followed after the cessation of the earthquake shaking. In the case with permeability $k = 3.3 \times 10^{-4} m/s$, the surface settlement was very small during the main shaking. Overall, it can be concluded from Fig. 12 that the settlement of the ground surface during the main shaking became increasingly marked with

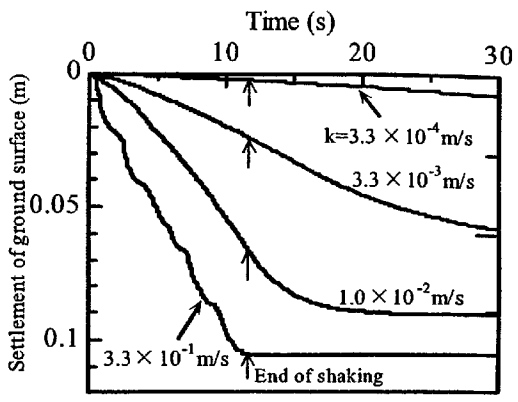

Fig. 12 Time histories of ground surface settlement

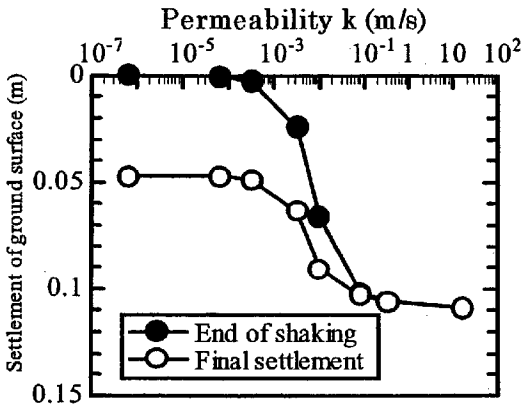

Fig . 13 Variations of seismic settlement and final settlement with permeabilities of soil

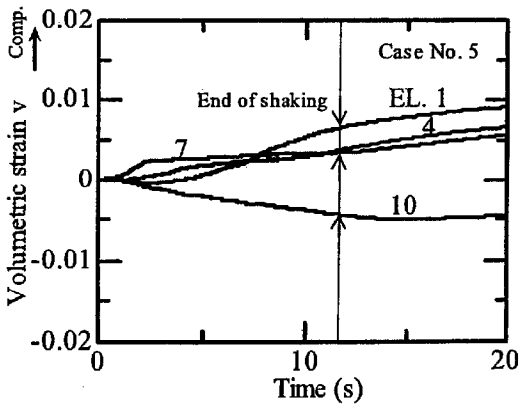

Fig. 14 Time histories of volumetric strains at four representative elements

increasing permeability.

The variations of the seismic settlements with the permeabilities of soil are summarized in Fig. 13. It is seen that with increasing permeability k,

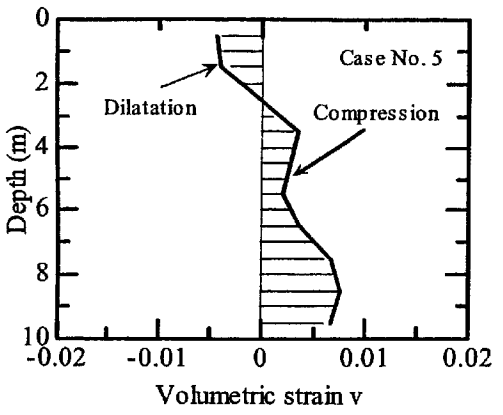

Fig. 15 Volumetric strain distribution with depth

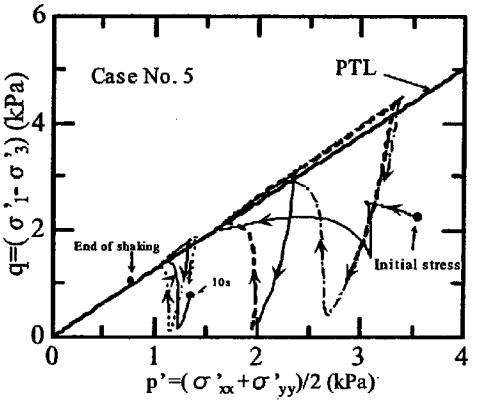

Fig. 16 Effective stress path at the shallow level (element No. 10) during main shaking

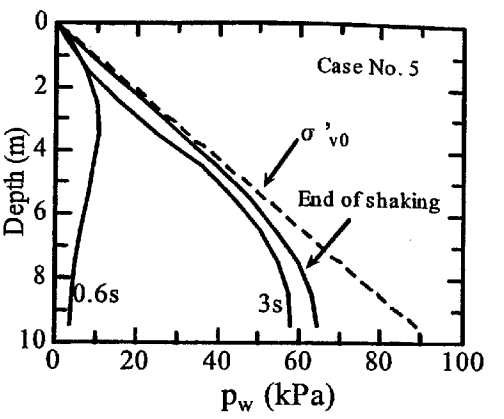

Fig. 17 Variations of excess pore pressures with depths

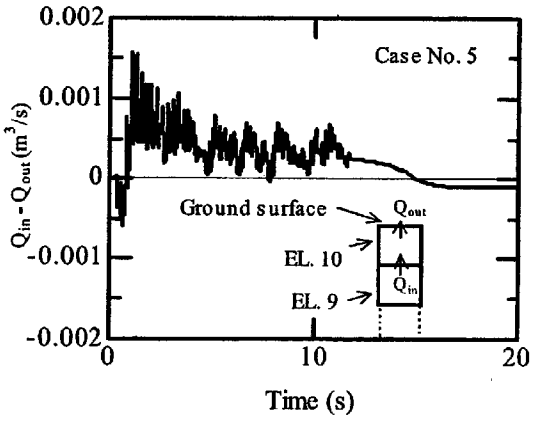

Fig. 18 Time history of the net discharge in element No. 10

the ground surface underwent larger seismic settlement during the main shaking.

The time histories of volumetric strains at four representative elements in Case 5 are shown in Fig. 14. The distribution of volumetric strains with depth in Case 5 is shown in Fig. 15. It is seen that compression strains developed at soil depths below 3m. At the shallower levels, however, the soil elements exhibited dilative behaviour during earthquake shaking.

In order to better understand this dilative behaviour in Case 5 at the shallow soil depths, we plotted the effective stress changes in element No. 10 in a form as shown in Fig. 16. In the first two loading cycles, the mean effective stress decreased gradually. Then the stress point crossed the phase transformation line, indicating dilatant behaviour.

The variations of excess pore pressures with depth in Case No. 5 is shown in Fig. 17. Close examination of the hydraulic gradients in the soil layer permitted the fluid budget to be worked out for each element. For instance, the time history of the net discharge, $Q_{in} - Q_{out}$, in element No. 10 is shown in Fig. 18. Here Q_{in} represents the rate of inflow from Element 9 below, and Q_{out} represents the rate of outflow from element No. 10 to the ground surface. Remember here that when $Q = Q_{in} - Q_{out} > 0$, the storage equation requires the element to expand. Indeed, the dilative soil behaviour observed in Element 10 is consistent with the pore pressure distributions obtained.

(2) Soil responses after cessation of shaking

The time histories of excess pore pressures in Case 2 during and post shaking are shown in Fig. 19. It is seen that the excess pore pressure dissipated gradually after the cessation of earthquake shaking. The variations of excess pore pressures

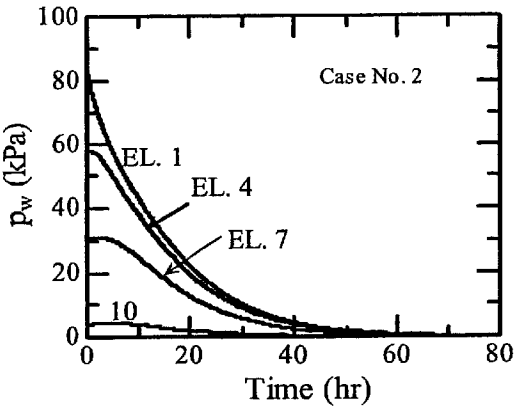

Fig. 19 Time histories of excess pore pressures

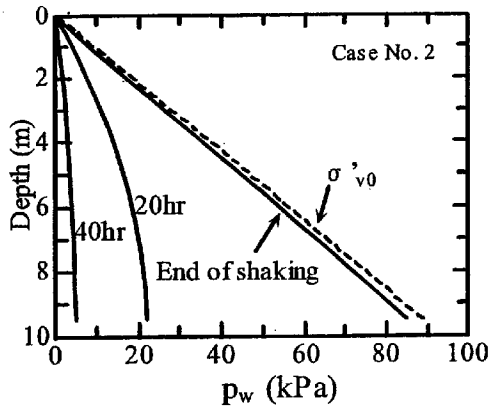

Fig. 20 The variations of excess pore pressures with depth after the cessation of earthquake shaking

with depth after the cessation of earthquake shaking in Case 2 are shown in Fig. 20 as various times. The excess pore pressures at deeper soil depths rapidly dissipated, but at the shallow level dissipation occurred at rather slow rates.

The final settlements obtained in all the cases are plotted in Fig.13 against the permeabilities of soil. It is seen that post-shaking consolidation settlement tends to increase in magnitude with decreasing permeability.

5. Conclusions

The elastoplastic behaviour of level ground subjected to SH waves under partially drained conditions, has been investigated using layer element modelling. The results obtained may be summarized as follows.

With increasing permeability, the ground surface settled increasingly faster, resulting in larger seismic settlements. However, the soil elements at shallow soil depths exhibited dilative behaviour. This may be ascribed to combined effects of dilatancy and upward pore fluid migration.

References

Akai, K. and Tamura, T. (1977): An application of nonlinear stress-strain relations to multi-dimensional consolidation problems. *Annuals, DPRI, Kyoto University*, No. 21 B-2, pp19-35 (in Japanese).

Arulannandan, K. and Scott, R. F. (1993): *Proc. of Int. Conf. on the Verification of Numerical Procedures for the Analysis of Soil Liquefaction Problems*, Vol. 1, Balkema.

Higuchi, Y., Tanizawa, F. and Sueoka, T. (1995): Method of liquefaction experiment by seismic centrifuge tests and considering experiment results, *Proceedings of the 50th annual conference of the Japan Society of Civil Engineers*, pp.552-553.

Pastor, M., Zienkiewicz, O.C. and Chan, A.H.C. (1990): Generalized plasticity and the modelling of soil behaviour. *Int. J. Numer. Anal. Methods Geomech.* Vol. 14, pp.151-190.

Port Bureau Ministry of Transport, Aviation Bureau Ministry of Trans-port. Ports and Harbor Research Institute in the Ministry of Trans-port, The 3rd District Port Construction Bureau Ministry of Trans-port , The Fishing Port Bureau Ministry of Fisheries, Civil Engineering Works in Hyogo Pref., Kobe-City Harbors Maintenance Bureau, Kobe Port Wharf Public Corporations. (1997): Damage report about harbors facilities due to 1995 Hyougoken-Nambu earthquake (In Japanese).

Sekiguchi, H., Kita, K., Hashimoto, K. and Katsui, H. (1996): Deformation of composite breakwa-

ters due to ground shaking, *Soils and Foundations*, Special Issue pp.169-177.

Simon, B. R., Zienkiewicz, O. C. and Paul, D. K. (1984): An analytical solution for the transient response of saturated porous elastic solids, *International Journal for Numerical and Analytical Methods in Geomechanics*, Vol. 8, pp.381-398.

Tatsuoka, F. and Ishihara, K. (1974): Drained deformation of sand under cyclic stresses reversing direction, *Soils and foundations*, Vol. 14, No. 3, pp. 51–65.

Yasuda,S., Nagase, H., Kiku, H. and Uchida, Y (1992): The Mechanism and a simplified procedure for the analysis of permanent ground displacement due to liquefaction, *Soils and Foundations*, Vol. 32, No.1, pp. 149-160.

Zienkiewicz, O. C., Chang, C. T. and Bettess, P. (1980): Drained, undrained, consolidating and dynamic behaviour assumptions in soils, *Géotechnique*, Vol. 30, No. 4, pp.385-395.

Appendix 1: Discretization of the equations of motion

The equations of motion (3) can be derived using the principle of virtual work.
The left-hand side on Eq. (3) stems from:

$$\int_V \delta u_i \rho \ddot{u}_i dV = \{\delta u_N\}^T \int_V [N]^T \rho [N] dV \{\ddot{u}_N\} \tag{49}$$

The first term on the right-hand side of Eq. (3) :

$$\begin{aligned}\int_V \delta u_i \sigma'_{ji,j} dV &= \int_V \{(\delta u_i \sigma'_{ji})_{,j} - \delta u_{i,j} \sigma'_{ji}\} dV \\ &= \int_A \delta u_i \sigma'_{ji} n_j dA + \{\delta u_N\}^T \int_V [B]^T \{\sigma'\} dV \\ &= -\{\delta u_N\}^T \int_A [N]^T \{T'\} dA \\ &\quad + \{\delta u_N\}^T \int_V [B]^T \{\sigma'\} dV \end{aligned} \tag{50}$$

where surface force T is expressed as $T = T' + T_p$. Here T' and T_p are the surface traction vectors for solid and pore fluid respectively.

The second term on the right-hand side of Eq. (3):

$$\begin{aligned}\int_V \delta u_i p_{,i} dV &= \int_V \{(\delta u_i p)_{,i} - \delta u_{i,i} p\} dV \\ &= \int_A \delta u_i p n_i dA + \{\delta u_N\}^T (\int_V [\nabla N]^T dV) p \\ &= -\{\delta u_N\}^T \int_A [N]^T \{T_p\} dA \\ &\quad + \{\delta u_N\}^T (\int_V [B_V]^T dV) p \end{aligned} \tag{51}$$

The third term on the right-hand side of Eq. (3) :

$$\int_V \delta u_i \rho b_i dV = \{\delta u_N\}^T \int_V [N]^T \rho \{b\} dV \tag{52}$$

Substituting Eqs. (49)-(52) into Eq. (3) yields

$$\begin{aligned}&\int_V [N]^T \rho [N] dV \{\ddot{u}_N\} + (\int_V [B]^T \{\sigma'\} dV \\ &+ \int_V [B_V]^T dV) p = \int_A [N]^T \{T\} dA \\ &+ \int_V [N]^T \rho \{b\} dV \end{aligned} \tag{53}$$

Since Eq. (53) holds for any time $t + dt$, one can rewrite Eq. (53) in the form:

$$\begin{aligned}&(\int_V [N]^T \rho [N] dV) \{\ddot{u}_N\}|_{t+dt} \\ &+ (\int_V [B]^T \{\sigma'\}|_{t+dt} dV) + (\int_V [B_V]^T dV) p|_{t+dt} \\ &= \int_A [N]^T \{T\} dA + \int_V [N]^T \rho \{b\} dV \end{aligned} \tag{54}$$

Similarly, Eq. (53) for time t takes the form:

$$\begin{aligned}&(\int_V [N]^T \rho [N] dV) \{\ddot{u}_N\}|_t + (\int_V [B]^T \{\sigma'\}|_t dV) \\ &+ (\int_V [B_V]^T dV) p|_t = \int_A [N]^T \{T\} dA \\ &+ \int_V [N]^T \rho \{b\} dV \end{aligned} \tag{55}$$

Subtracting Eq. (55) from Eq. (54) yields

$$\begin{aligned}&(\int_V [N]^T \rho [N] dV) \{\Delta \ddot{u}\} + (\int_V [B]^T \{\Delta \sigma'\} dV) \\ &+ (\int_V [B_V]^T dV) \Delta p = \int_A [N]^T \{\Delta T\} dA \\ &+ \int_V [N]^T \rho \{\Delta b\} dV \end{aligned} \tag{56}$$

The finite element equations that deal with a two phase medium may be expressed in matrix form, with constitutive relations (15) incorporated. Namely,

$$[M_{UU}]\{\Delta \ddot{u}_N\} + [K_{UU}]\{\Delta u_N\} + [K_{UP}]\Delta p = \{\Delta Q\} \tag{57}$$

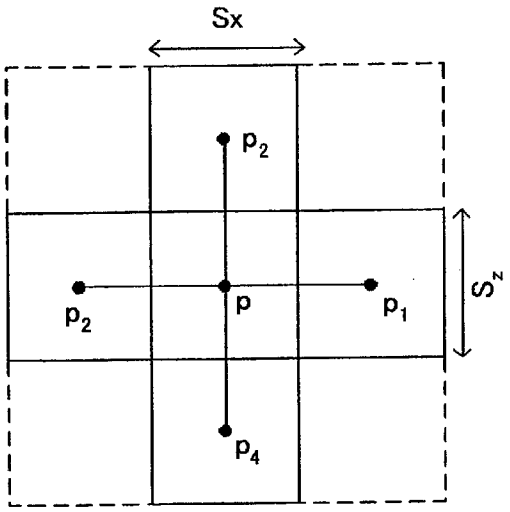

Fig. A1 Arrangement of a center element and four neighbouring elements to consider discretization of storage equation

where

$$[M_{UU}] = \int_V [N]^T \rho [N] dV \quad (58)$$

$$[K_{UU}] = \int_V [B]^T [D][B] dV \quad (59)$$

$$[K_{UP}] = \int_V [B_V] dV \quad (60)$$

$$\{\Delta Q\} = \int_A [N]^T \{\Delta T\} dA + \int_V [N]^T \rho \{\Delta b\} dV \quad (61)$$

Appendix 2: Discretization of the storage equation

Discretization of the continuity equation of pore fluid may be accomplished in a manner that is described below.

The left-hand side on Eq. (10) :

$$\int_V \rho_f \ddot{u}_{i,i} dV = (\int_V \rho_f [\nabla N] dV)\{\ddot{u}_N\} = (\int_V \rho_f [B_V] dV)\{\ddot{u}_N\} \quad (62)$$

The first term on the right-hand side of Eq. (10) :

$$\int_V p_{,ii} dV = \int_S p_{,i} n_i dS \quad (63)$$

The right-hand side on Eq. (63) :

$$\int_S p_{,i} n_i dS = \sum \frac{p_i - p}{L_i} S_i = \sum(\alpha_i' p_i) - \sum(\alpha_i') p \quad (64)$$

where $\alpha_i' = S_i / L_i$ and p is the pore fluid pressure at the center element(refer to Fig. 1).

The second term on the right-hand side of Eq. (10) :

$$\int_V \frac{\rho_f g}{k} \dot{u}_{i,i} dV = (\int_V \frac{\rho_f g}{k} \{\nabla N\} dV)\{\dot{u}_N\} = (\int_V \frac{\rho_f g}{k} [B_V] dV)\{\dot{u}_N\} \quad (65)$$

The third term on the right-hand side of Eq. (10) :

$$\int_V \frac{\rho_f g}{k} \frac{n}{K_f} \dot{p} dV = (\int_V \frac{\rho_f g}{k} \frac{n}{K_f} dV)\dot{p} \quad (66)$$

Substituting Eqs. (62)–(66) into Eq. (10), one can obtain the following:

$$(\int_V \rho_f [B_V] dV)\{\ddot{u}_N\} - (\int_V \frac{\rho_f g}{k} [B_V] dV)\{\dot{u}_N\} - (\int_V \frac{\rho_f g}{k} \frac{n}{K_f} dV)\dot{p} + \sum(\alpha_i' p_i) - \sum \alpha_i' p = 0 \quad (67)$$

For time $t + dt$, Eq. (67) takes the form:

$$\frac{\rho_f g}{k}\{\frac{k}{g}(\int_V [B_V] dV)\{\ddot{u}_N\}|_{t+dt} - (\int_V [B_V] dV)\{\dot{u}_N\}|_{t+dt} - (\int_V \frac{n}{K_f} dV)\dot{p}|_{t+dt} + \sum(\alpha_i p_i)|_{t+dt} - \sum \alpha_i p|_{t+dt}\} = 0 \quad (68)$$

Similarly for any time t, Eq. (67) becomes

$$\frac{\rho_f g}{k}\{\frac{k}{g}(\int_V [B_V] dV)\{\ddot{u}_N\}|_t - (\int_V [B_V] dV)\{\dot{u}_N\}|_t - (\int_V \frac{n}{K_f} dV)\dot{p}|_t + \sum(\alpha_i p_i)|_t - \sum \alpha_i p|_t\} = 0 \quad (69)$$

Subtracting Eq. (69) from Eq. (68) yields

$$\frac{\rho_f g}{k}\{\frac{k}{g}(\int_V [B_V] dV)\{\Delta\ddot{u}_N\} - (\int_V [B_V] dV)\{\Delta\dot{u}_N\} - (\int_V \frac{n}{K_f} dV)\Delta\dot{p} + \sum(\alpha_i \Delta p_i) - \sum \alpha_i \Delta p\} = 0 \quad (70)$$

Multiplying Eq. (70) by $k/(\rho_f g)$ permits the finite element equation for pore fluid to be expressed as

$$\frac{k}{g}(\int_V [B_V] dV)\{\Delta\ddot{u}_N\} - (\int_V [B_V] dV)\{\Delta\dot{u}_N\} - (\int_V \frac{n}{K_f} dV)\Delta\dot{p} + \sum(\alpha_i \Delta p_i) - \sum \alpha_i \Delta p = 0 \quad (71)$$

where $\alpha_i = \frac{k}{\rho_f g}\alpha_i'$.

要　旨

本研究では、SH波の鉛直入射に対する水平飽和砂層の弾塑性応答を有限要素解析に基づいて調べている。すなわち、横ひずみゼロという単純せん断条件を組み込んだ薄層要素を新たに導入し、一連の準一次元解析を部分排水条件のもとで行っている。土の繰返し塑性構成式としては、Pastorモデルの平面ひずみヴァーションを用いている。土の透水係数kを幅広く変えた一連の解析を行い、飽和砂層の地震時沈下の発達特性を明らかにしている。地盤の中央部および深部では常に圧縮沈下傾向となるにもかかわらず、地盤の浅部では土のダイレイタンシーと上向き浸透流の複合作用によって、膨張体積ひずみが発生しうることを指摘している。

キーワード： 繰返し塑性、液状化、部分排水効果、地震時沈下、単純せん断